Spin-triplet supercurrents of odd and even parity in nanostructured devices

Lahabi, K.

Citation

Lahabi, K. (2018, December 4). *Spin-triplet supercurrents of odd and even parity in nanostructured devices*. *Casimir PhD Series*. Retrieved from https://hdl.handle.net/1887/68031

Author: Lahabi, K.
Title: Spin-triplet supercurrents of odd and even parity in nanostructured devices
Issue Date: 2018-12-04

3

TRIPLET COOPER PAIRS IN MAGNETIC HYBRIDS

3.1. PROXIMITY EFFECT

PROXIMITY EFFECT is a general term used to describe the phenomena which occur at the interface between two different orders. We begin this section with a basic example, where a conventional (singlet) superconductor (S) is sharing an interface with a nonmagnetic normal metal (N), illustrated in Figure 3.1. At the interface the superconducting condensate $\Psi(\mathbf{R})$ extends into its adjacent layer, making it superconducting by proxy. In other words, despite the absence of an attractive interaction, there is still a finite probability of finding Cooper pairs in the normal metal. One can therefore think of this as the “leakage” of Cooper pairs into an adjacent medium.

As shown in Figure 3.1, deep within the superconductor the pair amplitude is at its maximum $\Psi(\mathbf{R} \to -\infty) = \Psi_0$, while on the other side of the interface, in the normal metal, the condensate must ultimately drop to zero $\Psi(\mathbf{R} \to +\infty) = 0$. Proximity effect is concerned with the region in between, where $|\Psi|$ falls as a function of distance. The characteristic length scale over which the order parameter can vary its amplitude is called the coherence length ξ, which is a material property. At the interface, Cooper pairs are depleted from the superconductor over a distance defined by $\xi_\mathrm{S}(T) \approx \xi(0)(1/\sqrt{T/T_\mathrm{c} - 1})$, where $\xi(0)$ corresponds to the coherence length of the superconductor at $T = 0$ K. Depending on the material, the value of $\xi(0)$ can vary from a couple of nanometer (cuprates) up to over a micron (Aluminium).[1]

---

[1] It is worth noting that Al is a rather extreme example. For most superconductors $\xi(0)$ is less than 200 nm.

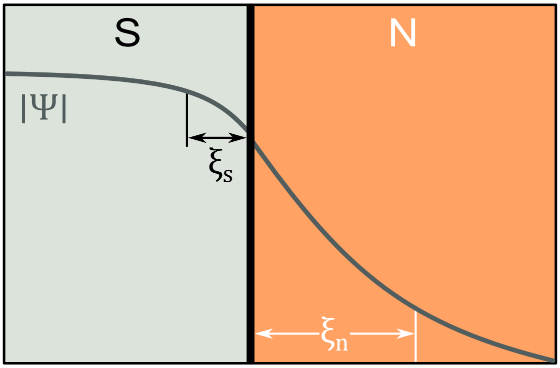

Figure 3.1: Proximity effect at the interface between a superconductor (S) and a normal metal (N). As the condensate Ψ spreads across the interface, its amplitude decays over the length scales ξ_s and ξ_n.

On the other side of the interface, the amplitude of Ψ falls over the characteristic length of ξ_n. In a diffusive system (dirty limit), defined by $\xi_\mathrm{n} < l$, where l is the mean fee path of the electron, ξ_n is given as

$$\xi_\mathrm{n} = \sqrt{\frac{\hbar D_\mathrm{n}}{k_\mathrm{B} T}} \tag{3.1}$$

where $\hbar$ is the Planck constant, D_n is the diffusion coefficient of the normal metal and k_B is the Boltzmann constant. For a transparent interface, this length scale is typically 100s of nm. While ξ_s and ξ_n may correspond to widely different values, the total condensate remains conserved. i.e. for every pair injected into the normal metal, a pair is “drained” from the superconductor.

So far we have described the proximity effect in terms of a macroscopic order parameter. There is however an equivalent microscopic description which concerns Andreev reflections. In this process an incident electron (hole) from N, with an energy below the superconducting gap, is retroreflected at the interface as a hole (electron) with equal and opposite momentum. The Andreev reflected electrons and holes result in a phase-coherent transport in units of $2e$, which is equivalent to transferring Cooper pairs across the interface. Likewise, the electron-hole pairs can maintain their phase-coherence in the normal metal over a characteristic distance which depends on the energy of the electron (hole) with respect to the Fermi energy, but on average, corresponds to ξ_n.[2]

---

[2] For more details on Andreev process see Refs. [1, 2].

3.1.1. SPIN-ACTIVE INTERFACES

Consider now replacing the normal metal with a ferromagnetic layer (F). The main difference with a normal metal is the exchange field of the ferromagnet E_{ex}, which splits the electronic bands for up and down spins by shifting their energy by $2E_{\mathrm{ex}}$. The singlet Cooper pair consists of two electrons with equal and opposite spins $(\uparrow,\downarrow)$ and momenta $(\mathbf{k}_f, -\mathbf{k}_f)$. This means a pair has a total spin and momentum of zero. By splitting the Fermi surface, the exchange field introduces a shift in momenta for spin up $\mathbf{k}_{f\uparrow} = \mathbf{k}_f + \mathbf{Q}/2$ and spin down $\mathbf{k}_{f\downarrow} = \mathbf{k}_f - \mathbf{Q}/2$ electrons (see Figure 3.2 **a**). In the diffusive limit, the shift corresponds to $Q = 2E_{\mathrm{ex}}/(\hbar v_f)$, where v_f is the Fermi velocity. This results in a finite momentum for $|\uparrow\downarrow\rangle$: $\mathbf{k}_{f\uparrow} - \mathbf{k}_{f\downarrow} = \mathbf{Q}$, and similarly for $|\downarrow\uparrow\rangle$: $\mathbf{k}_{f\downarrow} - \mathbf{k}_{f\uparrow} = -\mathbf{Q}$. The singlet state is then transformed into the linear combination of terms with different momenta

$$\frac{1}{\sqrt{2}}(|\uparrow\downarrow\rangle - |\downarrow\uparrow\rangle) \quad \longrightarrow \quad \frac{1}{\sqrt{2}}\left(|\uparrow\downarrow\rangle\, e^{i\mathbf{R}.\mathbf{Q}} - |\downarrow\uparrow\rangle\, e^{-i\mathbf{R}.\mathbf{Q}}\right) \tag{3.2}$$

which can be simplified to

$$\frac{1}{\sqrt{2}}\left[\Big(|\uparrow\downarrow\rangle - |\downarrow\uparrow\rangle\Big)\cos(\mathbf{R}.\mathbf{Q}) \quad + \quad i\Big(|\uparrow\downarrow\rangle + |\downarrow\uparrow\rangle\Big)\sin(\mathbf{R}.\mathbf{Q})\right]. \tag{3.3}$$

The first term is an oscillating singlet state $|0,0\rangle$ with zero spin ($S = 0$), while the second term describes a triplet state $|1,0\rangle$ ($S = 1$), whose spin projection is zero ($m = 0$) with respect to the spin quantization axis, which is defined by the direction of the exchange field of the ferromagnet. This spatially inhomogeneous singlet-triplet mixture (shown in Figure 3.2 **b**) is the equivalent of the famous FFLO state[3], which was originally intended as a possibility for *bulk* ferromagnetic superconductors [3, 4].

These correlations however can only survive in the F layer within a finite length scale from the interface. In a diffusive system (relevant to our structures) all pair amplitudes decay exponentially over ξ_{f}, which is given by

$$\xi_{\mathrm{f}} = \sqrt{\frac{\hbar D}{E_{\mathrm{ex}}}} \tag{3.4}$$

---

[3] Also known as the LOFF state, it is named after Peter Fulde and Richard Ferrell [3], and Anatoly Larkin and Yurii Ovchinnikov [4], who independently proposed the idea in connection with the coexistence problem of superconductivity with ferromagnetism. More details on this can be found in Refs. [5, 6]

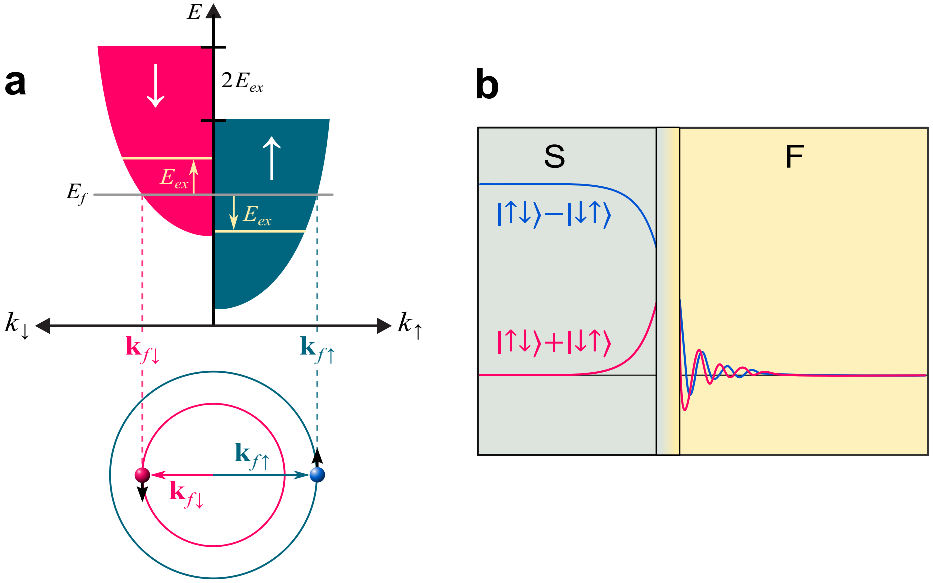

Figure 3.2: Cooper pairs at S-F interface: short-range proximity effect. **a** Spin polarization of the ferromagnet splits the bands for spin up (blue) and spin down (red) electrons by $2E_\text{ex}$ at the Fermi surface E_f, and leads to a shift in their momenta. This results in a finite momentum of the Cooper pair ($\mathbf{k}_{f\uparrow} \neq -\mathbf{k}_{f\downarrow}$). **b** singlet (blue)-triplet (red) mixing at the S-F interface. Spatially inhomogeneous singlet triplet mixture in the F layer corresponds to the FFLO state. In a diffusive ferromagnet with strong spin polarization, the correlations decay exponentially over $\xi_\text{f} \approx 1-5$ nm. The reflections from F layer cause spin-dependent phase shifts on the other side of the interface, forming a singlet-triplet mixture in S.

Unlike ξ_n, which was mostly determined by thermal processes, the value of ξ_f is dominated by the exchange energy E_ex. To gain some perspective, we can roughly translate E_ex to the Curie temperature, which is typically in the order of 100s of Kelvin. This means that in strong ferromagnets like Co and Ni, all correlations die out within $3-5$ nm from the interface— hence the name short-range proximity effect. The stronger the spin-polarization, the more suppressed the FFLO state is in the ferromagnet. At the same time however, stronger spin-polarization would have a larger impact on the superconducting side, where it induces an $m = 0$ triplet component (see Figure 3.2 **b**). This triplet component is a product of spin-dependent scattering phase shifts at the interface, which grow larger with the spin-polarization of F.

The exchange field results in different scattering phase delays for different spins ($\phi_\uparrow, \phi_\downarrow$). The corresponding phase shift can be expressed in terms of a *spin-mixing angle*, defined as $\theta = \phi_\uparrow - \phi_\downarrow$. In case of Cooper pairs, θ corresponds to the phase difference between a spin-up electron with momentum $\mathbf{k}$, and a spin-down with $-\mathbf{k}$, where $\mathbf{k}$ and $-\mathbf{k}$ point towards and away from the interface respectively. This results in a phase shift of θ for $|\uparrow\downarrow\rangle$, and $-\theta$ for $|\downarrow\uparrow\rangle$. The singlet state is hence converted to

$$\frac{1}{\sqrt{2}}(|\uparrow\downarrow\rangle - |\downarrow\uparrow\rangle) \quad \longrightarrow \quad \frac{1}{\sqrt{2}}\Big(|\uparrow\downarrow\rangle\, e^{i\theta} - |\downarrow\uparrow\rangle\, e^{-i\theta}\Big) \tag{3.5}$$

and can be written as

$$\frac{1}{\sqrt{2}}\Big[\Big(|\uparrow\downarrow\rangle - |\downarrow\uparrow\rangle\Big)\cos(\theta) \quad + \quad i\Big(|\uparrow\downarrow\rangle + |\downarrow\uparrow\rangle\Big)\sin(\theta)\Big] \tag{3.6}$$

In analogy to the formation of the FFLO state, we again arrive at a mixture of singlet $|0,0\rangle$ (first term) and triplet pairs $|1,0\rangle$ (second term) with no spin projection. The distinction here is that, instead of a momentum, the pair acquires a phase shift θ. The angle θ describes the rotation of the spin components *perpendicular* to the quantization axis under reflection. More importantly, we can consider θ as a measure of singlet-triplet mixing, which is a crucial ingredient for generating long-range triplet correlations.

3.1.2. LONG-RANGE TRIPLET CORRELATIONS

Given their capacity to generate $m = 0$ triplet correlations, it is natural to wonder if a spin-active interface can also provide the other triplet states $|\uparrow\uparrow\rangle$ and $|\downarrow\downarrow\rangle$ ($m = \pm 1$). Such correlations correspond to equal-spin pairing of the electrons, which puts them in a particularly interesting position. The reason for this is that pairs with parallel spin alignment are almost immune to the usual destructive influence of the exchange field, and can therefore lead to long-range superconducting correlations which are also spin-polarized. This provides an attractive prospect for spintronic applications, where decoherence and dissipation can be substantially minimized.

In order to proceed, consider the case where F and S are separated by a magnetic interface, whose magnetization vector $\mathbf{M}_i$ can vary with respect to that of the F layer $\mathbf{M}_\mathrm{F}$ (see Figure 3.3). The thickness of the interface region is restricted to values close to its ξ_f. For simplicity, we assume the interface and F are both highly spin-polarized, and therefore refrain from including the damped FFLO state in the sketches.

When $\mathbf{M}_i \parallel \mathbf{M}_\mathrm{F}$ (Figure 3.3 **a**), the system is practically equivalent to a single S-F interface. Inside the ferromagnet, the FFLO state leads to a mixture of spatially oscillating singlet and $m = 0$ triplet components. These correlations are faced with the problem of populating spin-split Fermi surfaces, and therefore only last for atomically small distances. However, there is also singlet-triplet mixing in the S layer, as a result of spin-dependent phase shifts that occur during reflections from the F layer. Interestingly, these correlations can reach up to 10s of nm, as their characteristic length scale

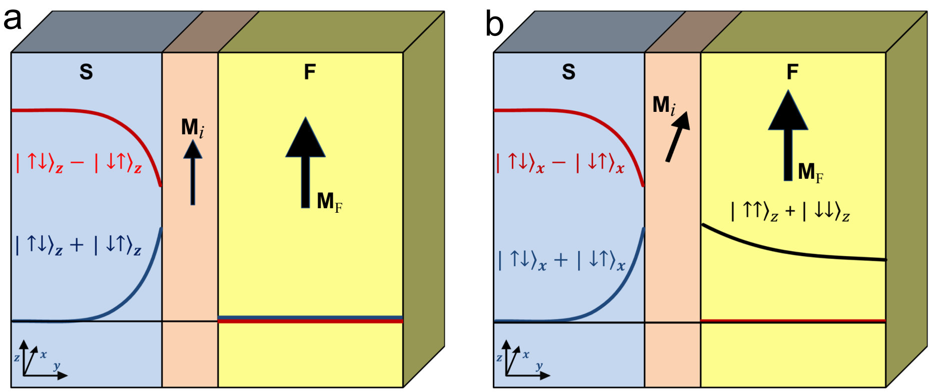

Figure 3.3: Generating equal-spin triplet pairs at S-F interface: long-range proximity effect. **a**, magnetization of the interface $\mathbf{M}_i$ and that of the F layer $\mathbf{M}_\mathrm{F}$ are aligned with z. Spin quantization axis for triplet-singlet mixing is z, and the correlations are suppressed in the F layer. **b**, if $\mathbf{M}_i \parallel x$, the $|\uparrow\downarrow\rangle_x + |\downarrow\uparrow\rangle_x$ triplet has zero spin-projection along x, but can decompose into $|\uparrow\uparrow\rangle_\mathrm{z}$ and $|\downarrow\downarrow\rangle_\mathrm{z}$ as we switch the quantization axis to z in F. The equal-spin pairs are not broken by the exchange field, leading to long-range proximity.

is defined by the size of the Cooper pairs i.e. the coherence length of the superconductor ξ_s. However, this triplet state cannot survive in the ferromagnet as it also has zero spin-projection along z, and therefore suffers the same fate as the FFLO phase.

Let us now consider the case where $\mathbf{M}_i$ makes an angle with $\mathbf{M}_\mathrm{F}$ (shown in Figure 3.3 **b**). For simplicity, we assume $\mathbf{M}_\mathrm{F}$ to align with the z-axis within the F layer, while $\mathbf{M}_i$ points along the x-axis. The spin-mixing that occurs in the S layer is therefore a result of the exchange field in the x-direction. In contrast to Figure 3.3 **a**, the spin quantization of the singlet-triplet mixture at the interface is now defined with respect to the x-axis. While the triplet state $|\uparrow\downarrow\rangle_\mathrm{x} + |\downarrow\uparrow\rangle_\mathrm{x}$ has zero spin-projection in x-direction, it can decompose to $|\uparrow\uparrow\rangle_\mathrm{z}$ and $|\downarrow\downarrow\rangle_\mathrm{z}$ pairs in the F layer. Due to their equal spins, such pairs do not “feel” the exchange field of the ferromagnet. These triplet correlations can therefore spread through the ferromagnet, just as singlet pairs do in a normal metal. By the same token, the characteristic decay length for equal-spin triplets is given by

$$\xi_\mathrm{f}^\mathrm{ESP} = \sqrt{\frac{\hbar D_\mathrm{f}}{k_\mathrm{B} T}} \tag{3.7}$$

which is equivalent to the expression for ξ_n (3.1). As a result, the typical length scale for equal-spin triplet Cooper pairs in a ferromagnet can exceed far beyond the value of ξ_f. For a strong ferromagnet such as Co, $\xi_\mathrm{f}^\mathrm{ESP}$ is in the order of 10s of nm, but it can also reach values as large as a micron in case of the half-metallic ferromagnet CrO$_2$. Furthermore, the amplitude of equal-spin pairing is proportional to the magnetic non-collinearity at the interface. In the above example (Figure 3.3 **b**), we assumed the magnetization of the interface to be perpendicular to that of the F layer. This corresponds to the maximum amplitude of long-ranged triplets generated. Besides amplitude, the orientation of the magnets also determines the phase of the triplet correlations. This is discussed in Section 3.1.4 in connection with π- and φ-junctions.

Supercurrents (triplet as well as singlet) are generally studied in the context of a basic device known as the Josephson junction. It is therefore necessary to introduce the general Josephson effect before proceeding further with the discussion on triplet correlations in S-F hybrids.

3.1.3. JOSEPHSON EFFECT

The Josephson effect is concerned with the overlap of two macroscopic wavefunctions that are separated by some form of weak link. The concept is illustrated in Figure 3.4**a**, which shows two superconducting electrodes, each corresponding to a distinct wavefunction described by $\Psi_{l,r} = ne^{i\phi_{l,r}}$. Here n is the density of Cooper pairs, which we assume to be the same for the left (l) and right (r) electrodes, and $\phi_{l,r}$ corresponds to the macroscopic quantum phase of individual condensates. The two wavefunctions can extend over the weak link and couple with each other through proximity effect. On the other hand, Ψ_l and Ψ_r can have different phases, and in order to transfer Cooper pairs between the electrodes, phase coherence must be maintained. Josephson showed that the supercurrent across a junction is determined by this phase difference through

$$I = I_\text{c}\sin(\varphi) \tag{3.8}$$

where $\varphi = \phi_l - \phi_r$, and I_c is the maximum amount of supercurrent the junction can sustain. Below this value transport is dissipationless, and characterised with zero voltage V (i.e. resistance). The nonlinear current-voltage characteristic of a typical junction is shown in Figure 3.4**b**, where the system is biased with a d.c. current. The Josephson relation 3.8 also demonstrates an important distinction between superconductors and normal conductors. Conventional electronics are governed by the Ohm's law, which states that electrical current is driven by the voltage ($I \propto V$). In a superconducting circuit however, there is no potential difference ($V = 0$). Instead, the current is driven by the phase difference φ. What makes the macroscopic phase of fundamental importance is that it means electrical transport in a superconductor has a wave-like nature. This can be confirmed by the behaviour of a single Josephson junction in presence of a magnetic field. As shown in Figure 3.4 **c**, $I_\text{c}(B)$ follows a Fraunhofer "diffraction pattern", similar to that of a wave passing through a narrow slit. In analogy with optics, the total supercurrent that can flow in one direction is modulated by the spatial variations of the phase. The difference is that here the

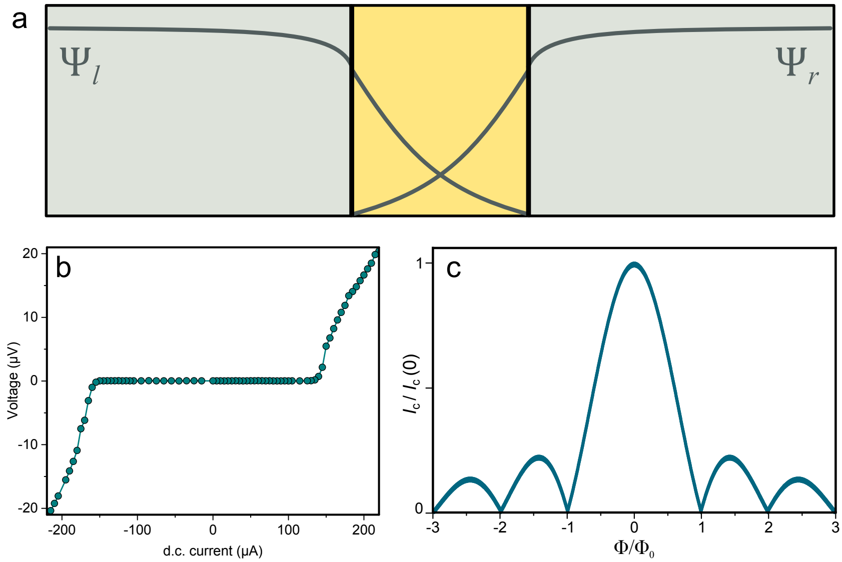

Figure 3.4: Josephson effect. **a**, schematic of a Josephson junction. A weak link (yellow) is proximized by the overlapping wavefunctions $\Psi_{l,r}$ of the superconducting electrodes. **b**, typical $I-V$ characteristic of Josephson junction. The plateau corresponds to the zero resistance (i.e. static phase). **c**, Fraunhofer pattern (simulated), representing the basic relation between critical current (normalised) and applied magnetic flux in a standard Josephson junction.

phase variation is introduced by the magnetic flux threading the junction Φ. Since flux can only enter a superconductor in quantised units, the supercurrent diffraction is described by

$$I_c(B) = I_c^{\max}\left|\frac{\sin\left(\frac{\pi\Phi}{\Phi_0}\right)}{\frac{\pi\Phi}{\Phi_0}}\right| \tag{3.9}$$

where $\Phi_0 = \hbar/2e$ is the magnetic flux quantum (fluxoid), and $I_c^{\max}$ is the maximum critical current of the junction.

In the same way ξ is the characteristic length for the amplitude of the order parameter, a characteristic length (λ) can be assigned to the phase of the order parameter. Hence, generally speaking, λ can be described as the length scale over which ϕ can vary. This definition of can be applied to any superconducting system, and is not limited to Josephson junctions.[4] Given that supercurrent is driven by the phase difference, λ is also the characteristic length for supercurrent amplitude. For instance, under an external magnetic field, the circulating currents inside a superconductor are restricted to a finite range. As the supercurrent amplitude decays over λ, so does the magnetic field, which is the reason for referring to λ as the penetration depth.

---

[4] Not to be confused with the λ_J, which is specific to Josephson junctions.

There are however multiple variations of λ, each applicable to a different system i.e. a bulk superconductor would correspond to a different λ than the one for a thin film or a Josephson barrier. The bottom line here is that the phase of the order parameter can only vary over a finite length scale, which is determined by λ. Also, as we describe in later chapters, external magnetic fields are not the only means of creating a phase difference.

3.1.4. LONG-RANGE TRIPLET SUPERCURRENTS

The theoretical developments on long-range proximity effects began by a series of consecutive papers in the beginning of 2000s [7–9]. In their pioneering work, Sebastián Bergeret, Anatoly Volkov and Konstantin Efetov studied S-F structures where the magnetization rotates near the interface. They showed such systems can produce equal-spin triplet amplitudes which can extend over long distances in the ferromagnet. More surprisingly however, was that they found these triplet correlations to have even-parity (s-wave) and odd-frequency. This was the same pairing state that Berezinskiĭ [10] had proposed in 1974 for superfluid ^{3}He, which later was found to be p-wave (even-frequency). This rather unexpected development had important symmetry implications. The realization of equal-spin pairing with s-wave symmetry meant the order parameter is robust against elastic scattering from non-magnetic impurities. Therefore, spin-polarized supercurrents can propagate through ordinary ferromagnetic films, even when transport is diffusive. This is to be distinguished from p-wave triplets (even frequency), which are restricted to clean materials [11].

A crucial aspect of the theory of the odd-frequency triplets was that it relied strongly on the presence of a certain type of magnetic inhomogeneity at the interface. It was clear that without this, spin-mixing could not produce the s-wave triplet correlations. This led to an on-going series of theoretical proposals for generating, and controlling, long-range triplet correlations in various S-F hybrid systems. The early theoretical studies considered the use of domain walls [7, 12–16] and spiral magnetic structures [17–20] as possible candidates for triplet spin-mixing. Sosnin *et al.* attempted to realise these ideas using the intrinsic helical magnetic phase of holmium [21]. The authors applied Andreev interferometry to investigate transport through a Ho wire (50 – 150 nm long) contacted by superconducting electrodes. They observed Φ_0-periodic conductance oscillations, which indicated phase-coherent superconducting transport through the Ho wire. A Josephson current however was not detected. The wires maintained appreciable resistance which, below a certain point, did not seem to decrease by lowering the temperature— indicating the junctions were most likely not fully proximized.

An important experimental evidence of long-range triplet supercurrent came in 2006, where Keizer *et al.* reported supercurrents through the half-metallic ferromag-

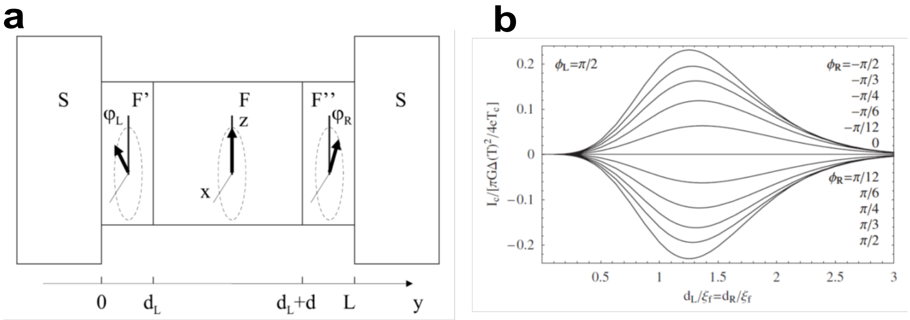

Figure 3.5: Generating long-range triplet current with a magnetic trilayer. **a** Schematic of an S/F'/F/F"/S junction. Arrows indicate the magnetic orientation of each layer. Magnetization of the middle F layer (thickness = d) is fixed along z, while F' and F" (thicknesses d_L and d_R) can rotate their magnetizations by φ_L and φ_R respectively. **b** Normalised I_c as a function of layer thickness d_L (d_R), plotted for various orientations of φ_R, while fixing $\varphi_L = \pi/2$. I_c amplitude is maximum for $\varphi_R = \pm\pi/2$ i.e. if F' and F" magnetizations are both perpendicular to the magnetization in F. Negative (positive) I_c corresponds to the π (zero) state. Taken from Ref. [30].

net CrO_2 [22]. They observed a finite supercurrent between NbTiN electrodes that were separated by over 300 nm on a CrO_2 film. Given the fully spin-polarized nature of CrO_2 (only one spin type has a conduction band, and the other is insulating) [23–28], this was a strong evidence of a long-range triplet component with equal-spin pairing of electrons. Their experiments however could not provide any information about the frequency of orbital symmetry of the correlations. As transport in the CrO_2 film may still be in the clean limit, where an odd-parity order parameter could survive, it was therefore not possible to determine whether the triplet pairing was of odd-frequency (s-wave) or odd-parity (p-wave) type. Furthermore, the results of Keizer *et al.* proved rather difficult to reproduce. It was only in 2010 that Anwar *et al.* succeeded in reproducing the effect using MoGe electrodes separated by 700 nm on CrO_2 film [29]. This was partly due to the difficulties in making transparent interfaces with CrO_2, which is metastable and reduces to Cr_2O_3 at room temperature. This forms an insulating layer, which needs to be carefully removed from the surface of CrO_2 before depositing any electrical contacts. The other difficulty however was the lack of control over magnetization at the interface with the CrO_2 films. As described in section 3.1.2, the presence of a certain magnetic inhomogeneity at the interface is crucial for generating long-range odd-frequency triplet pairing. However, the source of magnetic inhomogeneity in the early CrO_2 devices was rather ambiguous and difficult to control.

A major breakthrough was made in 2007 by Houzet and Buzdin who proposed a device structure to generate (and potentially control) triplet supercurrents in multilayer systems [30]. Their proposal was based on a Josephson junction where the weak link consisted of a ferromagnetic trilayer (S/F/'F/F"/S), where the magnetization of F' and F” could be rotated with respect to F (see Figure 3.5 **a**). They showed that the amplitude of long-range triplet supercurrent is maximum if F’ and F” are magnetized perpendicular to F, and vanishes if they are collinear (i.e. when F’ and F” are either parallel or antiparallel to F). Equally important was that the relative alignment of the F’ and F” also determined if the junction is in a 0 or π state. They showed that if the F’ and F” are parallel, the junction has an intrinsic phase of $\varphi = \pi$ (i.e. is a π-junction), while in the antiparallel configuration $\varphi = 0$ (see Figure 3.5 **b**). Hence, in addition to controlling the amplitude of supercurrent, the magnetic orientation of the layers can be used to realise both 0 and π states in the same device. This was recently demonstrated in Ref. [31], where the phase of a triplet junction, with a multilayer weak link, could be switched between 0 and π by turning the magnetization of one layer by 180°.

Note that even before the emergence of long-range triplet devices, π-junctions had been realized by short-range proximity effect in thin (< 10 nm) and weakly spin-polarized ferromagnets. In such systems the crossover between 0 and π was usually achieved by carefully varying the thickness of the ferromagnet or, under very specific circumstances, by varying the temperature [5, 32]. In terms of device applications, neither of these options could match the robustness of a triplet junction, such as the one depicted in Figure 3.5. This led to a growing interest in the use of magnetic multilayers for singlet to triplet conversion. Shortly after, a series of experimental efforts succeeded in realizing this, and long-range triplet currents were found in a number of multilayer junctions — using different materials and device configurations.

As shown in Figure 3.5 singlet to triplet conversion with a multilayer requires non-collinear magnetization of the ferromagnets. In practice however, realising such magnetic configuration is by no means a trivial task. The difficulties arise from the fact that local interlayer coupling tends to favour parallel or antiparallel alignment of the magnetizations [5]. While interlayer exchange interactions can be regulated with nonmagnetic spacers, interlayer dipolar (magnetostatic) coupling has proven to be rather problematic. This has been a major hurdle for the controlled generation of triplet correlations, and has been the focus of intensive studies [33–37]

The individual groups which succeeded in generating long-range triplet currents, each had a distinct method to overcome this issue. Robinson *et al.* implemented the conical magnetic configuration of holmium to create non-collinearity with cobalt magnetization in Nb-Ho-Co-Ho-Nb nano-pillar junctions (see Figure 3.6 **a**,**b**) [38]. Meanwhile Khaire *et al.* developed a different approach using a synthetic antiferromagnetic interlayer (SAF) made of a Co-Ru-Co trilayer [39]. In this case, the exchange coupling through Ru leads to antiparallel alignment of magnetic domains in the adjacent Co layers, thereby suppressing their demagnetising fields. The SAF decouples the Co magnetization from the other ferromagnets in a S-F’-N-SAF-N-F’-S

---

[5] More on this in Section 3.2 where we examine multilayer systems with micromagnetic simulations

stack used in their devices (See Figure 3.6 **c**,**d**), allowing a magnetic non-collinearity to be present between Co and F' layers. The multilayer convertor was also implemented by Anwar *et al.* , where they extended their work on CrO_2 junctions [40]. Using MoGe-Ni(1.5 nm)-Cu(5 nm) electrodes, deposited on a CrO_2 film, they found critical currents that were about two orders of magnitude higher than their previous works. This was a strong indication of spin-mixing by magnetic misalignment, and consistent with the behaviour of odd-frequency triplets.

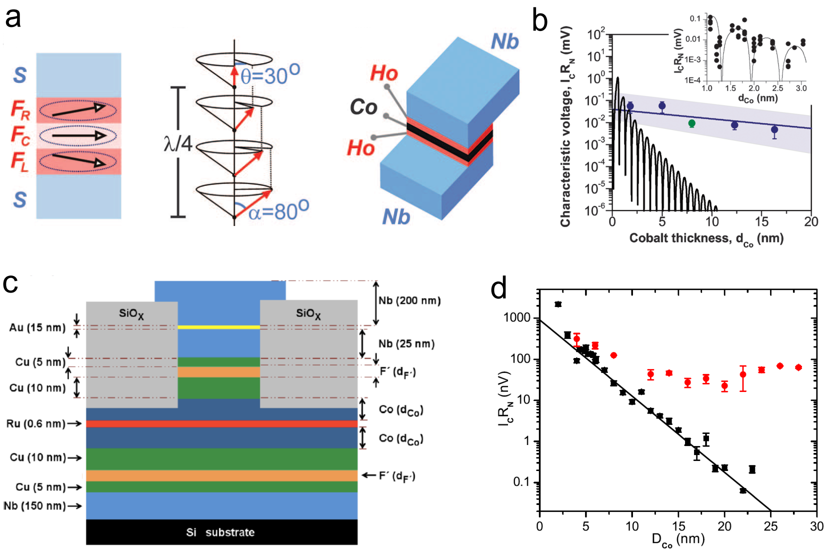

Figure 3.6: **a**, configuration of the Ho/Co/Ho trilayer used in Ref. [38], where the conical magnetic structure of Ho was used to inject long-range triplet correlations into Co. Magnetic moments of Ho (red arrows) rotate by $\theta = 30°$ per atomic layer, leading to a spiral with a period of $\lambda \approx 3.4\ nm$. **b**, normalised I_c as a function of Co thickness. The oscillating curve is the simulated behaviour for short-range proximity, where I_c would be rapidly suppressed. Instead, the the measured I_c falls as if the Co barrier was nonmagnetic. Taken from Ref. [38]. **c**, schematic of the magnetic multilayer used for generating long-range triplet current in Ref [39]. Here, the magnetic "trilayer" consists of one (Co/Ru/Co) and two separate PdNi (4 nm) layers, shown here as F'. **d**, I_c as function of Co thickness for junction with (red circle) and without (black square) the F' layers. For the full trilayer, there is no appreciable decay of I_c for Co thicknesses up to 30 nm. Taken from Ref. [34].

Besides non-collinear multilayers, there is a growing number of proposals for generating and controlling triplet correlations which remain unexplored. A number of these ideas revolve around the use of spin "texture". This corresponds to systems where two; or all three components of magnetization (m_x, m_y, m_z) vary spatially in at least two dimensions. The spatial variation of the magnetization needs to take place over a certain length scale that is comparable to ξ_f. These conditions can be realised in the magnetic ordering of certain mesoscopic ferromagnets and magnetic domain walls.

3.2. MICROMAGNETIC SIMULATIONS

3.2.1. MICROMAGNETIC THEORY

The magnetic state of any given structure can be modelled by finding the state that corresponds to lowest free energy. The magnetic energy however consists of a number of discrete components. In systems described here, the most relevant energy terms are the exchange, anisotropy, demagnetizing (also called magnetostatic energy) and Zeeman. The total energy is then determined by the sum of all energy densities, integrated over the volume of a system.

$$E_{\text{tot}} = \int_V (\varepsilon_{\text{ex}} + \varepsilon_{\text{anis}} + \varepsilon_{\text{demag}} + \varepsilon_{\text{z}}) dV \tag{3.10}$$

Consider calculating this for the relatively simple 3-dimentional system shown in Figure 3.7 **b**. On the atomic scale the exchange interaction aligns the neighbouring magnetic moments, while on a larger scale the demagnetizing term forces the magnetic moments to align with the sample boundaries to minimize stray fields. Nevertheless, depending on the exact geometry, there will be a presence of demagnetizing fields which results in dipole interactions between the adjacent ferromagnets. In addition to these, there are also the contributions from magnetic anisotropy, which can be different for each material, and external magnetic fields.

There is no doubt that an analytical approach to this problem would be overwhelmingly complex and tedious. Fortunately however, the micromagnetic theory allows us to implement numerical methods that are far more effective. Instead of considering individual magnetic moments, the micromagnetic theory postulates that magnetization (i.e. magnetic moments per unit volume) is a spatially continuous function **M**(**r**) [41]. Based on this approximation a system can be divided into discrete units

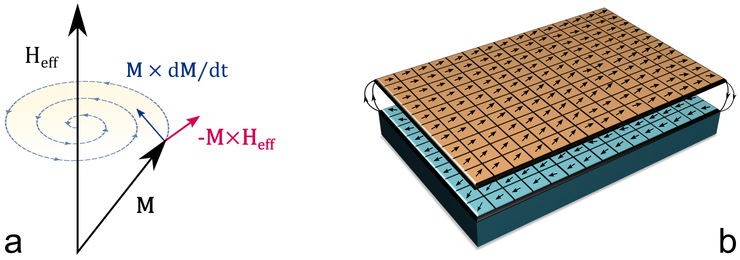

Figure 3.7: **a** Precession (red) and damping (blue) of magnetization vector **M** under an effective magnetic field $\mathbf{H}_{\text{eff}}$, as described by LLG 3.12. **b** Micromagnetic theory applied to a magnetic multilayer. System is divided into discrete cells, where each unit can be assigned with a magnetization vector **m**, which is subject to a local effective field. This also includes stray fields, which lead to interlayer dipolar coupling (shown as solid lines connecting the layers).

of finite dimensions. Each segment is described by a unit magnetization vector, and experiences a local effective field $\mathbf{H}_{\text{eff}}(\mathbf{r})$ given by

$$\begin{aligned} \varepsilon_{\text{tot}} &= -\int \mu_0 \mathbf{H}_{\text{eff}}(\mathbf{r}).\mathbf{M}(\mathbf{r}) d^3 r \\ \mathbf{H}_{\text{eff}}(\mathbf{r}) &= -\frac{1}{\mu_0} \nabla_{\mathbf{M}} \varepsilon_{\text{tot}} \end{aligned} \tag{3.11}$$

Hence, all the components of magnetic energy are now elegantly represented by single magnetic field. This enables us to obtain the *dynamic* magnetization of each cell by solving the time-dependent Landau-Lifshitz-Gilbert (LLG) equation

$$\frac{d\mathbf{M}}{dt} = \gamma\mu_0 \mathbf{M} \times \mathbf{H} - \frac{\alpha}{M_s} \mathbf{M} \times \frac{d\mathbf{M}}{dt} \tag{3.12}$$

where γ is the gyromagnetic ratio and α is the Gilbert damping parameter. Here, the first term describes the procession of **M** in a local effective field, while the second term corresponds to dissipation (see Figure 3.7 **a**). Solving the LLG for every cell, one by one, over the entire system, and in many iterations, allows each unit of magnetization to interact with its neighbouring cells and reconfigure its direction over time. The overall magnetization therefore "evolves" by minimizing its total energy, until the system relaxes into a minimum in the free energy landscape.

3.2.2. SIMULATIONS

The simulations are carried out using the object-oriented micromagnetic framework (OOMMF) software package [42], which applies finite element techniques to the differential LLG equation 3.12. It works discretising a given object over a small mesh, where at each point LLG is solved and integrated using Runge-Kutta algorithms [43] to calculate the magnetization. It is possible to define the anisotropy and initial magnetization of individual cells, and vary an applied field over the entire object. It also calculates the demagnetizing fields using Fast-Fourier-transformations [44, 45].

The equilibrium state can be found by monitoring the rate at which magnetization changes its direction. In the Runge-Kutta evolver this is represented by the parameter $|d\mathbf{m}/dt|_{\text{max}}$, which has units of degrees per nanosecond, where $\mathbf{m}$ is the unit magnetization direction. Preferably, the value of $d\mathbf{m}/dt$ should be as small as possible. Depending on the individual system, we set $|d\mathbf{m}/dt|_{\text{max}} < 0.1$, which means the simulation will stop if the maximum magnetization derivative of each cell is less than 0.1 degrees per nanosecond. A typical simulation can take somewhere between

10^5 to 10^6 iterations and, in some cases, may not converge at all. Even with the high-performance clusters of 48 - 64 cores, this could correspond to days, and sometimes weeks, of computational time. It is therefore critical to choose our computational parameters carefully, and monitor the evolution of magnetization at every stage to ensure the simulation is progressing in consistent manner.

The mesh size is one of the crucial parameter which should be chosen carefully. In most cases, but not always, a smaller cell size provides a more realistic representation of a given object. One the other hand, increasing the number of cells could overwhelmingly slow down the simulation. As a rule, this value needs to be of the order of the exchange length, given by

$$l_{\mathrm{ex}} = \sqrt{\frac{2A}{\mu_0 M_s^2}} \tag{3.13}$$

where A is the exchange stiffness in units of J/m. In general, l_{ex} can be described as the characteristic length scale over which the magnetic moments can change their alignment in presence of an exchange field. For strong ferromagnets this value is in the order of 5 nm, which is also the standard mesh size used in our simulations. Another important parameter for convergence is the damping constant α in LLG 3.12. This can be interpreted as a measure of how quickly the field and magnetization align (see Figure 3.7 **a**). As we are mainly interested in the equilibrium state, we set $\alpha = 0.5$ for rapid convergence. Using smaller values would substantially increase the simulation time and hardly affect the equilibrium state.

As stated earlier, OOMMF allows defining the magnetic anisotropy of the individual cells. This can be set to represent the appropriate magnetocrystalline anisotropies (e.g. uniaxial for cobalt and cubic for nickel etc.). However, with the exception of CrO_2, the ferromagnetic films used in this work are prepared by sputter deposition on amorphous SiO_2 substrates. To represent the polycrystalline nature of these films, where each grain has an arbitrary orientation, we use a random vector field to set the principal axes of each unit cell. Since magnetocrystalline anisotropy is now smeared out in all directions, shape anisotropy (the minimization of the stray fields) becomes the dominant factor. For the sputtered films of Co and Ni used here, this leads to an in-plane magnetisation with no specific easy axes. This anisotropy was also confirmed by our ferromagnetic resonance (FMR) and SQUID magnetometry [46].

Crystallinity and geometry however are not the only factors which can result in a magnetic anisotropy. In some cases, certain deposition conditions can also result in a preferred magnetic direction. An example of this is the permalloy (Py) films deposited in presence of a finite magnetic field, which can develop an out-of-plane anisotropy [47]. In this case, experiments were necessary to determine the anisotropy, which we could then use as input in our simulations — and model the individual domain structures found in the patterned Py films.

In addition to anisotropy, simulations also require the exchange stiffness A and saturation magnetization M_s. These values are provided in the OOMMF database (commonly used in literature). We found the reported values for M_s to be in close agreement with the ones obtained from our FMR and SQUID measurements.

3.2.3. MULTILAYER PLANAR JUNCTIONS

In this section we describe how micromagnetic simulations can be applied to multilayers to design optimal planar junctions with long-range triplet current (see Figure 3.8). Ideally we need a stable magnetic non-collinearity (MNC) between F and F' layers, which can also be modified and controlled by applying external magnetic fields. For our devices, we will be using Ni (1.5nm) and Co (50-60 nm) as the F and F' respectively. The ferromagnets are separated by a Cu(5 nm) layer to avoid interlayer exchange coupling. The thickness of the Ni layer was found to be optimal for triplet generation in similar multilayer systems [34, 48].

We begin by examining a bar-shaped device, which is the standard configuration of planar Josephson junctions. This is typically realised a rectangular multilayer strip, where the superconducting layer can in some way be discontinued to create a weak link. In our devices, this would mean opening a gap in the top Nb-Ni-Cu layers, leaving only Co in the weak link.

Figure 3.9 **a** shows the plane view of Co and Ni magnetizations at zero field, obtained from 3-D OOMMF simulations. The pixel colour scheme, red-white-blue, scales with the magnetization along x. In order to estimate the MNC, for each cell at the top of the Co layer we determine the angle θ between its magnetization vector and that of the Ni cell above (see Figure 3.9 **b**). From this we can extract a MNC profile over the entire structure, shown in Figure 3.9 **c**. We observe a pronounced cou-

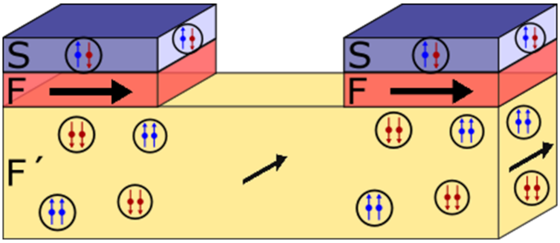

Figure 3.8: Schematic representation of a planar multilayer junction. To generate long-range triplet current, F and F' layers must have non-collinear magnetizations.

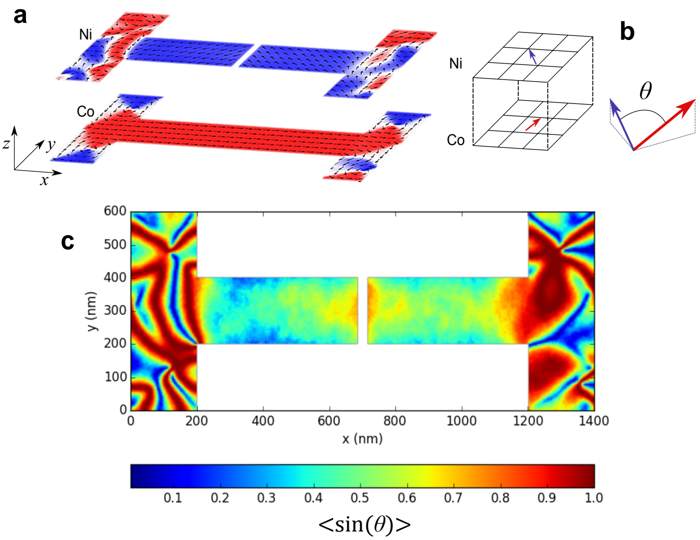

Figure 3.9: **a**, Plane view magnetization of Co(45 nm) and Ni (2 nm) at zero applied field, obtained from 3D OOMMF simulations. The gap in Ni corresponds to the location of weak link is. The pixel colour scheme, red-white-blue, scales with the magnetization along x. **b** represents our method to obtain the MNC profile shown in **c**. For each cell at the top of the Co layer, θ is determined by the angle between the magnetization vector of Co and that of the Ni cell above. $<\sin(\theta)>$ is defined as the absolute value of the outer product between the Co and Ni magnetization vectors (note that the colour scheme is different from **a**).

pling between the ferromagnets, with an antiparallel configuration being the magnetic ground state. This has a detrimental effect on the MNC in the junction, which is clearly visible in Figure 3.9 **c**.

To better understand the nature of the interlayer interactions we performed film dependent simulations, where the magnetizations are reversed by sweeping an in-plane field. An example of this is shown in Figure 3.10. Initially, both Co and Ni are fully magnetized by a large magnetic field applied in $-x$ direction. As we sweep the field towards zero, the Co magnetization remains relatively unchanged. Meanwhile, Ni begins to reverse its magnetization around −100 mT — which switches its direction to $+x$ already at $\mu_0 H = -15$ mT. This is a result of local dipole fields from Co, which begin to dominate the effective field acting on Ni when the applied field is not substantial. The antiparallel configuration continues up to $\mu_0 H = 65$ mT, at which point Co reverses its magnetization to $+x$. While we observe some adjustments in the Ni magnetization, for the most part it remains along $+x$, and parallel to Co.

We found the interlayer dipole coupling to be consistently present in all bar-shaped junctions studied, even when the boundaries were extended to reduce the effects of stray fields Figure 3.9 **c**. In such systems only the parallel and antiparallel magnetic configurations are stable, both equally undesirable for generating triplet currents.

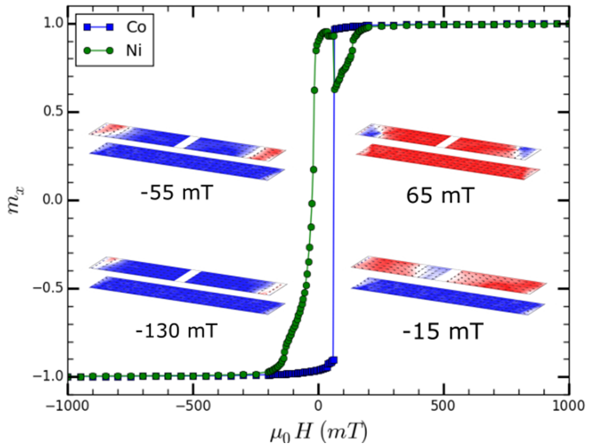

Figure 3.10: Simulation of the magnetization reversal in a bar-shaped Co(45 nm) / Ni(1.5 nm) bilayer. The field is swept from −1 T to 1 T, taking 5 mT field steps within ± – 200 mT. Individual magnetizations of Co (blue squares) and Ni (green circles) layers are plotted separately. The insets show snap-shots of Co (bottom) and Ni (top) at different stages of magnetization reversal.

Even if the ferromagnets could somehow be decoupled and form a non-collinear state, their stray fields could still be a serious issue for the junction. Most SFS junctions are known to suffer from stochastic self-fields which lead to distorted and/or shifted interference patterns, and other unwanted irregularities [33–37].

In order to resolve these issues altogether, we implemented a disk-shaped design to create a vortex magnetization in the Co layer. As shown in Figure 3.11, the curled structure of a ferromagnetic vortex is highly effective in minimizing stray fields. Furthermore, the vortex magnetization is fully in-plane except for the core, where it sharply turns out of plane. The core has a local magnetization of $\mu_0 M_s \approx 1.8$ T. Despite its large value, due to the small radius of the core $(5 - 10$ nm) [49], this field corresponds to a relatively small flux $\approx 10 - 20\ \%\Phi_0$.

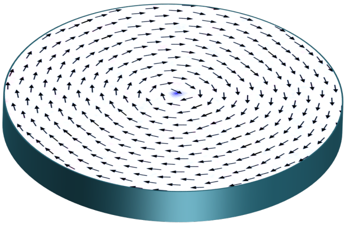

Figure 3.11: **Ferromagnetic vortex**. Simulated magnetic pattern of a 50 nm thick Co disk with 1 μm diameter. At the vortex core the magnetic moments turn sharply out-of-plane (blue pixels).

The position of the core can be varied in a coherent manner using in-plane magnetic fields. Moreover, the magnetic anomaly at the core is expected to suppress long-range triplet correlations [50]. We therefore can utilize the core as the means to gain dynamic control over the distribution of triplet current. This concept is described in detail in Chapters 4 and 5.

3.3. CrO_2 NANOWIRES

In this section we present an alternative to the S/F'/F/F"/S trilayer, the conventional device configuration for generating triplet supercurrent. This is realised by implementing the domain structure of mesoscopic CrO_2 crystals. We begin by describing the micromagnetic pattern of various CrO_2 nanowires.

3.3.1. MAGNETIC PATTERNS

The magnetic structure of a crystalline CrO_2 wire is a product of magnetocrystalline and shape anisotropies. The former is a uniaxial anisotropy which favours the magnetization to align with the [001] axis of the crystal, while the latter serves to minimise the demagnetizing energy by aligning the magnetic moments along the wire (i.e. the long side of the structure). These two terms can be exploited to obtain widely different magnetic states in CrO_2. We realise this with the help of selective area growth, where a SiO_x mask, deposited on a TiO (100) substrate, can be used to define the shape and orientation of individual CrO_2 crystals (see Figure 3.12 **a**). Sample prepration and the growth of crystalline CrO_2 wires are described in Ref. [51].

If grown along [001], the wire would be aligned with the magnetic easy axis of the crystal. In this case both anisotropies favour the magnetization to lie parallel to the wire. When a wire is sufficiently narrow ($w \lesssim 2$ μm), it would have a highly uniform magnetization where $M \parallel [001]$. In such systems, domain walls are typically scarce, since a transverse component of magnetization would be unfavourable by both anisotropies. This uniform magnetic structure has been utilized in some of our wire CrO_2 wire junctions to create a non-collinear magnetization with a Ni layer at the interface with the superconducting electrodes, which were deposited on the wire (perpendicular to its axis) [51].

If a is wire grown along [010], which is the hard axis of CrO_2, its magnetic structure will be entirely different. In this case, shape anisotropy prefers the magnetization to lie along the wire ($M \parallel [010]$), while the magnetocrystalline anisotropy favours

---

* The work presented in this section is to be submitted for publication.

Author contributions: samples were prepared by Amrita Singh. Kaveh Lahabi and Louis Maduro did the micromagnetic simulations. Transport measurements were carried out by Amrita Singh and Kaveh Lahabi. Jan Aarts supervised the project.

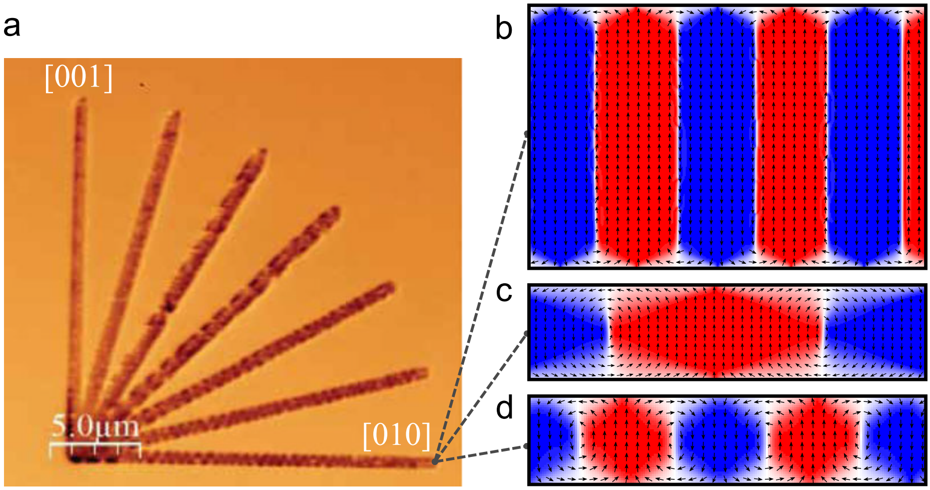

Figure 3.12: Magnetic patterns of CrO_2 crystals: **a** Magnetic force microscopy images of CrO_2 bars, grown along various directions [51]. **b**, **c** and **d** show the micromagnetic simulations for the 2 μm, 0.5 nm and 200 nm wide wires, respectively, grown along [010]. The pixel colour scheme, red-white-blue, scales with the (positive-zero-negative) magnetization along the easy axis of the crystal, which is transverse to the wire. Note that **b**, **c** and **d** correspond to different magnifications (wires in **c** and **d** are enlarged for clarity). In all simulations presented here, we set the wires to be 10 μm long and 104 nm thick. The cell size is (8 nm× 8 nm× 8 nm) for the 2 μm wide wire, and (5 nm× 5 nm× 5 nm) for the rest.

the magnetization to be perpendicular to it. The resulting magnetic pattern would then be a compromise, corresponding to their relative energies. While the crystalline anisotropy maintains a fixed value (2.7×10^4 J/m^3), the shape anisotropy can be tuned by varying the lateral dimensions of the bar.

Figure 3.12 **b-d** present the simulated magnetizations for bars of various widths, grown along the hard axis of CrO_2. In the 2 μ m wide bar (3.12 **b**), we observe stripe-like domains where magnetization alternates transverse to wire. Within each domain the magnetization is relatively uniform except for the regions near the edges of the wire, where magnetic moments are rotated to reverse the magnetization between adjacent domains. This spatially continuous rotation of magnetization is a consequence of the shape anisotropy, whose role to minimize dipole (stray) fields by turning the magnetic moments parallel to the surface of the bar. The shape anisotropy becomes more dominant by reducing the width of the bar. This leads to the emergence of an array of magnetic vortices in the 500 nm and 200 nm wide wires.

A vortex is characterised by two independent parameters: chirality, defined by the in-plane winding of magnetization (left or right), and polarity, set by the out-of-plane magnetization (up or down) located of the vortex core. Usually the vortices in ferromagnetic nanowires are isolated or, in certain circumstances, apear as pairs (see for example Refs. [52, 53]). More importantly, in almost every case they are a form

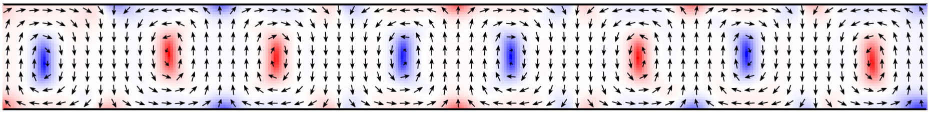

Figure 3.13: Simulated magnetic pattern of a 200 nm wide CrO_2 wire grown along [010]. The pixel colour scheme, red-white-blue, scales with the out-of-plane magnetization. The wire hosts a series of magnetic vortices with well-defined cores. The adjacent vortices have opposite chiralities.

of domain wall: separating two larger segments with uniform magnetizations. Interestingly however, here we observe a continuous array of adjacent vortices (see Figure 3.13). Unlike the stripe domains in the 2 μm wide bar (Figure 3.12 **b**), there is no clear distinction between a domain and a domain wall.[6]

This unusual state leads to a particular type of magnetization reversal which, to the best of our knowledge, has so far has been exclusive to magnetic disks [7]. These systems are characterized by a vortex core that can be displaced in a highly coherent and reversible manner, with no remnant magnetization. This results in a peculiar type of hysteresis loop, as shown in Figure 3.14.

The simulations in Figure 3.14 describe the magnetization reversal of a 5 μm$\times$200 nm CrO_2 bar, grown along the hard magnetic axis of the crystal. It also illustrates the magnetization patterns at various stages of the reversal. We begin by magnetizing the sample with a large magnetic field, applied in the $-y$ direction, which is transverse to the wire, and parallel to the easy axis of CrO_2 ($y \parallel [001]$). At **A** the wire is uniformly magnetized by the applied field. As we reduce the field, magnetic moments begin to align themselves with the sides of the wire, and magnetization begins to buckle. This trend continues up to **B**, after which point the pattern breaks down into a series of vortices distributed along the wire. At zero field (**C**) we find the vortices to be uniformly spaced. This results in zero remnant magnetization, since m_y has the same magnitude in $\pm y$. As we switch the field direction (**D**), a $+y$ magnetization begins to develop by displacing vortices along the wire (perpendicular to the applied field). By increasing the field, one or two vortices are driven out from the ends of the wire. The rest however end up as pairs, and are locked in to each other. This is because of the opposite chirality of adjacent vortices, which drives in them in different directions under the applied field. The motion of each vortex is therefore blocked by one of its neighbours, travelling in the opposite direction. As magnetization grows, vortex displacement begins to halt as the pairs are pushed against each other. This trend continues until they cannot get any closer to each other (**E**), at which point they vanish by spontaneously switching their magnetization.

---

[6] Note that we also found no vortex cores in the 2 μm wide bar.

[7] Here, we have also included the wires where multiple vortices can be stacked on top of each other [54, 55].

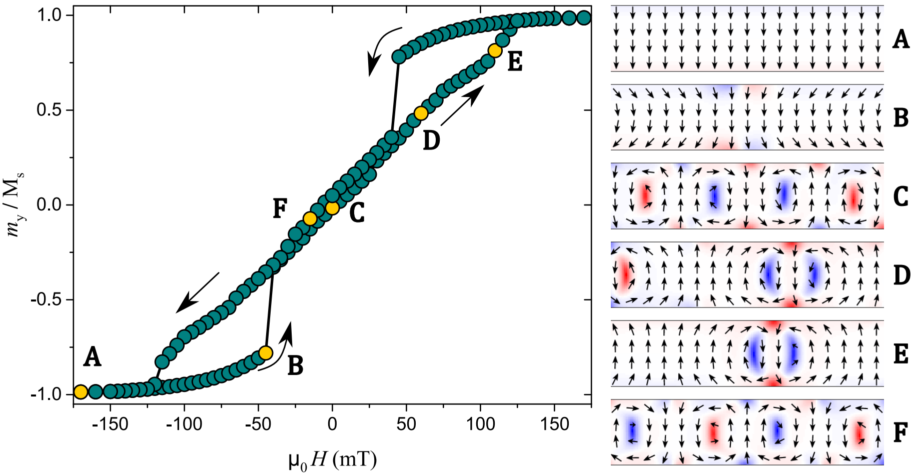

Figure 3.14: The simulated $M-H$ loop of a 200 nm wide wire, together with the magnetization patterns at various stages of vortex revesal.

As we magnetize the wire along $+y$ and bring the field back to zero, the magnetization goes through the equivalents of **A** and **B**. Lastly, at **F** we see a similar pattern as **C**. Even though the system was fully magnetized in the opposite direction, there is no sign of a remnant magnetization when we compare **F** with **C**.

In a magnetic disk, the field would push the vortex core (in a perpendicular direction) to one side of the disk, where it begins to slow down as it approaches the edge. This continues until the vortex cannot get any closer to the edge and vanishes in a single transition. Hence, vortex displacement is restricted solely by the geometry of the disk and its physical boundaries. In a wire however, there are no geometrical restrictions to stop a vortex from moving along its axis, which is why (domain wall) vortices in a typical ferromagnetic wire yield an entirely different type of magnetization reversal. Remarkably, here we find vortex chirality to play the role of sample boundary: the motion of a vortex is stopped by one of its adjacent vortices, as it would have been by the edge of a disk.

Note also that there is no particular relation between the polarity and/or the chirality of vortices in **F** and **C**. This is because the symmetries of the reversal process described above; do not favour a particular chirality or polarity over the other. The two parameters are therefore nondeterministic during a magnetization reversal.

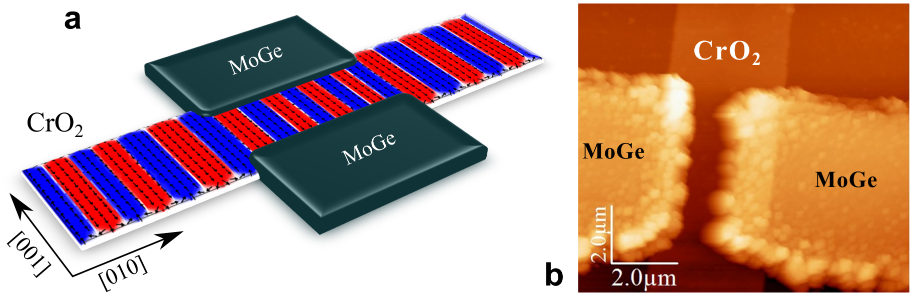

Figure 3.15: **a**, schematic of a transverse junction where the magnetic barrier consists of a single 2 μm wide CrO$_2$ bar with stripe domains. The pixel colour scheme, red-white-blue, scales with magnetization along [001]. **b**, scanning force microscopy image of the junction used in transport measurements of Figure 3.16. The superconducting MoGe electrodes contact the CrO$_2$ wire on both sides.

3.3.2. GENERATING LONG-RANGE TRIPLETS WITH MAGNETIC PATTERN

In addition to non-collinear multilayers, it has been proposed that long-range triplet correlations can also be generated by the magnetic pattern of a single ferromagnet [50, 56]. We demonstrate this in planar Josephson junctions, where the superconducting electrodes (MoGe) are deposited on the sides of a 2μm CrO$_2$ nanowire, as shown in Figure 3.15. Note that in this configuration; the transport direction is perpendicular to the axis of the wire. Here, the triplet correlations are generated by the exchange field gradient present on the sides of the wire with stripe domains. Although the contacts are separated by ≈ 500 nm, we a observe substantial critical current. At 2 K the supercurrent density is close to 4×10^9 A/m^2, see Figure 3.16 **a**.

At zero field, the system is in equilibrium. The stripes are about 500 nm wide and equally spaced, and the supercurrent is at its maximum. For the 2 μm wide bar however, our simulations indicate that the stripes can be modified by applying a relatively small in-plane field along the easy axis of CrO$_2$ (μ_0H ∥ [001]). They show that as we sweep the field from zero, the domains that are aligned with field direction (i.e. red stripes when the field is positive and blue stripes for negative fields) begin to increase in size, while the opposite domains shrink (see Figure 3.16 **a**). Taking field steps of 2 mT in our simulation, we find all domains to be magnetized by the field at 26 mT. This state corresponds to a relatively uniform magnetization with substantially less exchange field gradient, corresponding to minimum triplet generation. This is also supported by the transport measurements where we find no critical current above 20 mT. The reason for supercurrent vanishing even below the switching field is addressed below. First however, we make a note that the junction is relatively robust against out-of-plane fields. Even at fields as high as 600 mT the critical current maintains a finite value. This is because the stripe domains continue to be present until the bar is magnetized out-of-plane, and that requires substantially higher fields.

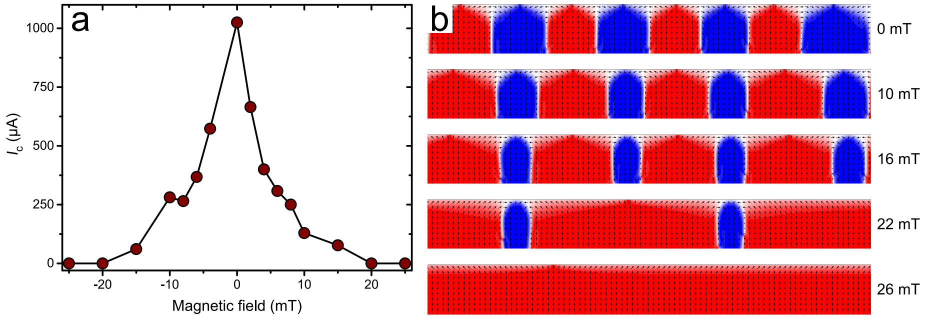

Figure 3.16: **a**, I_c measured as a function magnetic field, applied in the [001] direction i.e. along the stripe domains ($H \parallel I$). **b** , micromagnetic simulations for different applied fields, showing the magnetic pattern at the *edge* of the 2 μm-wide bar (full width shown in Figure 3.12 **b**), where the superconducting MoGe electrodes make contact with the CrO_2 wire. Red and blue correspond to parallel and antiparallel magnetizations, with respect to the direction of applied field.

It is evident that the junction transport strongly depends on the magnetic inhomogeneity – which is a key ingredient in generating long-range triplet correlations. For junctions with a single ferromagnetic barrier, spin-mixing is commonly associated with the exchange field gradient that is present at the magnetic domain walls (DWs). In our system however, the rotation of magnetization near the edges of the wire are arguably just as relevant (if not more) than the actual DWs.

The simulations show that magnetizing the sample would increase the size of one domain type over the other (e.g. red over blue or vice versa in Figure 3.16 b). The actual number of DWs however remains constant over a 3 μm-long segment of the wire (corresponding to the length of superconducting electrodes) up to 22 mT, where the minority domains begin to vanish by abruptly switching their magnetization from parallel to antiparallel to the field. Similarly, for small fields, there are no drastic changes in the overall magnetic texture of the wire. As shown in Figure 3.16 b), increasing the field to 10 mT barely changes the rotating magnetization pattern that appears near the edges. Hence, the rapid suppression of critical current cannot be entirely due to the lack of magnetic inhomogeneity for triplet generation. To appreciate the full picture, we consider what happens when we break the symmetry of parallel and antiparallel domains.

Unlike the 500 nm and 200 nm wide bars shown in Figure 3.12 **b**, the 2 μm bar does not contain magnetic vortices. While the stripe domains have may have chirality, there are no vortex cores with out-of-plane magnetization. Instead, we observe in-plane magnetic dipoles that form near the edge, in between the DWS. In equilibrium, the adjacent domains produce equal and opposite dipole fields, which cancel each other out over a few microns. However, applying a relatively small in-plane field can tip this balance by making one type of domain slightly larger than the other one. This leads to an effective local field which induces additional screening currents in the superconducting electrodes, which in turn lead to the suppression of critical current.

The upshot here is that micromagnetic simulations can be implemented to design a wide range of magnetic hybrids which can generate and control long-range triplet supercurrent. In the above example, the simulations were used to obtain detailed description of the local magnetization texture in a variety of CrO_2 structures. We showed that by making basic adjustments to the dimensions of a simple wire bar we can extract widely different magnetic states. Subsequently, the well-defined stripe domains of a 2 μm wide bar were used to inject high supercurrent densities in CrO_2, without the need for extra magnetic layers. Reducing the problem to a single ferromagnet plays a significant role in our ability to control the triplet current. Utilizing the robust nature of magnetization reversal in for these particular dimensions enables us to switch off all supercurrent with only a few mTs — which is a highly practical field range for device applications. It is also worth noting that the coercive field of the CrO_2 nanowires could be significantly enhanced by reducing their width.

We note that a vortex pattern, such as the one shown in Figure 3.13 should also be capable of generating triplet currents [50, 56]. This is the focus of Chapter 5, where we demonstrate how the exchange field gradient in a ferromagnetic disk can induce long-range triplet correlations in cobalt. Combining the exceptionally high supercurrent densities in crystalline CrO_2 wires with the coherent motion of magnetic vortices would offer a rich platform to study triplet Coopers in the nonequilibrium setting, which is necessary for magnetization dynamics and spin-transfer torque. This system becomes even more intersting if we consider the possibility of storing information (bits) with the polarity and chirality of individual vortices.

REFERENCES

[1] T. Klapwijk. Proximity effect from an Andreev perspective. *Journal of Superconductivity*, 17(5):593–611, 2004.

[2] C. W. Beenakker. Random-matrix theory of quantum transport. *Reviews of Modern Physics*, 69(3):731, 1997.

[3] P. Fulde and R. A. Ferrell. Superconductivity in a strong spin-exchange field. *Physical Review*, 135(3A):A550, 1964.

[4] A. Larkin and I. Ovchinnikov. Inhomogeneous state of superconductors (production of superconducting state in ferromagnet with Fermi surfaces, examining Green function). *Soviet Physics-JETP*, 20:762–769, 1965.

[5] A. I. Buzdin. Proximity effects in superconductor-ferromagnet heterostructures. *Reviews of Modern Physics*, 77(3):935, 2005.

[6] M. Eschrig. Spin-polarized supercurrents for spintronics: a review of current progress. *Reports on Progress in Physics*, 78(10):104501, 2015.

[7] F. Bergeret, A. Volkov, and K. Efetov. Long-range proximity effects in superconductor-ferromagnet structures. *Physical Review Letters*, 86(18):4096, 2001.

[8] A. Kadigrobov, R. Shekhter, and M. Jonson. Quantum spin fluctuations as a source of long-range proximity effects in diffusive ferromagnet-superconductor structures. *EPL (EuroPhysics Letters)*, 54(3):394, 2001.

[9] F. Bergeret, A. F. Volkov, and K. B. Efetov. Odd triplet superconductivity and related phenomena in superconductor-ferromagnet structures. *Reviews of Modern Physics*, 77(4):1321, 2005.

[10] V. Berezinskiĭ. New model of the anisotropic phase of superfluid ^{3}He. *JETP Letters*, 20(9):287–289, 1974.

[11] M. Eschrig, J. Kopu, J. Cuevas, and G. Schön. Theory of half-metal/superconductor heterostructures. *Physical Review Letters*, 90(13):137003, 2003.

[12] A. Konstandin, J. Kopu, and M. Eschrig. Superconducting proximity effect through a magnetic domain wall. *Physical Review B*, 72(14):140501, 2005.

[13] A. Volkov, A. Anishchanka, and K. Efetov. Odd triplet superconductivity in a superconductor/ferromagnet system with a spiral magnetic structure. *Physical Review B*, 73(10):104412, 2006.

[14] A. Volkov and K. Efetov. Odd triplet superconductivity in a superconductor/ferromagnet structure with a narrow domain wall. *Physical Review B*, 78(2):024519, 2008.

[15] A. Volkov, Y. V. Fominov, and K. Efetov. Long-range odd triplet superconductivity in superconductor-ferromagnet structures with Néel walls. *Physical Review B*, 72(18):184504, 2005.

[16] Y. V. Fominov, A. Volkov, and K. Efetov. Josephson effect due to the long-range odd-frequency triplet superconductivity in SFS junctions with Néel domain walls. *Physical Review B*, 75(10):104509, 2007.

[17] M. Alidoust and J. Linder. Spin-triplet supercurrent through inhomogeneous ferromagnetic trilayers. *Physical Review B*, 82(22):224504, 2010.

[18] C. Wu, O. T. Valls, and K. Halterman. Reentrant superconducting phase in conical-ferromagnet–superconductor nanostructures. *Physical Review Letters*, 108(11):117005, 2012.

[19] C. Wu, O. T. Valls, and K. Halterman. Proximity effects in conical-ferromagnet/superconductor bilayers. *Physical Review B*, 86(18):184517, 2012.

[20] J. Linder, T. Yokoyama, and A. Sudbø. Theory of superconducting and magnetic proximity effect in S/F structures with inhomogeneous magnetization textures and spin-active interfaces. *Physical Review B*, 79(5):054523, 2009.

[21] I. Sosnin, H. Cho, V. Petrashov, and A. Volkov. Superconducting phase coherent electron transport in proximity conical ferromagnets. *Physical Review Letters*, 96(15):157002, 2006.

[22] R. Keizer, S. Goennenwein, T. Klapwijk, G. Miao, G. Xiao, and A. Gupta. A spin triplet supercurrent through the half-metallic ferromagnet CrO_2. *Nature*, 439(7078):825, 2006.

[23] K. Schwarz. CrO_2 predicted as a half-metallic ferromagnet. *Journal of Physics F: Metal Physics*, 16(9):L211, 1986.

[24] J. Coey and M. Venkatesan. Half-metallic ferromagnetism: Example of CrO_2. *Journal of Applied Physics*, 91(10):8345–8350, 2002.

[25] S. P. Lewis, P. B. Allen, and T. Sasaki. Band structure and transport properties of CrO_2. *Physical Review B*, 55(16):10253, 1997.

[26] R. Soulen, J. Byers, M. Osofsky, B. Nadgorny, T. Ambrose, S. Cheng, P. R. Broussard, C. Tanaka, J. Nowak, J. Moodera, et al. Measuring the spin polarization of a metal with a superconducting point contact. *Science*, 282(5386):85–88, 1998.

[27] W. DeSisto, P. Broussard, T. Ambrose, B. Nadgorny, and M. Osofsky. Highly spin-polarized chromium dioxide thin films prepared by chemical vapor deposition from chromyl chloride. *Applied Physics Letters*, 76(25):3789–3791, 2000.

[28] Y. Ji, G. Strijkers, F. Yang, C. Chien, J. Byers, A. Anguelouch, G. Xiao, and A. Gupta. Determination of the spin polarization of half-metallic CrO_2 by point contact Andreev reflection. *Physical Review Letters*, 86(24):5585, 2001.

[29] M. Anwar, F. Czeschka, M. Hesselberth, M. Porcu, and J. Aarts. Long-range supercurrents through half-metallic ferromagnetic CrO_2. *Physical Review B*, 82(10):100501, 2010.

[30] M. Houzet and A. I. Buzdin. Long range triplet Josephson effect through a ferromagnetic trilayer. *Physical Review B*, 76(6):060504, 2007.

[31] J. A. Glick, V. Aguilar, A. B. Gougam, B. M. Niedzielski, E. Gingrich, R. Loloee, W. Pratt Jr, and N. O. Birge. Phase control in a spin-triplet SQUID. *arXiv preprint arXiv:1804.00707*, 2018.

[32] V. Ryazanov, V. Oboznov, A. Y. Rusanov, A. Veretennikov, A. A. Golubov, and J. Aarts. Coupling of two superconductors through a ferromagnet: Evidence for a π junction. *Physical Review Letters*, 86(11):2427, 2001.

[33] T. S. Khaire, W. Pratt Jr, and N. O. Birge. Critical current behavior in Josephson junctions with the weak ferromagnet PdNi. *Physical Review B*, 79(9):094523, 2009.

[34] M. A. Khasawneh, T. S. Khaire, C. Klose, W. P. Pratt Jr, and N. O. Birge. Spin-triplet supercurrent in Co-based Josephson junctions. *Superconductor Science and Technology*, 24(2):024005, 2011.

[35] V. Bol'ginov, V. Stolyarov, D. Sobanin, A. Karpovich, and V. V. Ryazanov. Magnetic switches based on Nb-PdFe-Nb Josephson junctions with a magnetically soft ferromagnetic interlayer. *JETP Letters*, 95(7):366–371, 2012.

[36] E. Gingrich, P. Quarterman, Y. Wang, R. Loloee, W. Pratt Jr, and N. O. Birge. Spin-triplet supercurrent in Co/Ni multilayer Josephson junctions with perpendicular anisotropy. *Physical Review B*, 86(22):224506, 2012.

[37] M. Blamire, C. Smiet, N. Banerjee, and J. Robinson. Field modulation of the critical current in magnetic Josephson junctions. *Superconductor Science and Technology*, 26(5):055017, 2013.

[38] J. Robinson, J. Witt, and M. Blamire. Controlled injection of spin-triplet supercurrents into a strong ferromagnet. *Science*, 329(5987):59–61, 2010.

[39] T. S. Khaire, M. A. Khasawneh, W. Pratt Jr, and N. O. Birge. Observation of spin-triplet superconductivity in Co-based Josephson junctions. *Physical Review Letters*, 104(13):137002, 2010.

[40] M. Anwar, M. Veldhorst, A. Brinkman, and J. Aarts. Long range supercurrents in ferromagnetic CrO_2 using a multilayer contact structure. *Applied Physics Letters*, 100(5):052602, 2012.

[41] W. F. Brown Jr. Thermal fluctuations of a single-domain particle. *Physical Review*, 130(5):1677, 1963.

[42] M. J. Donahue. OOMMF user's guide, version 1.0. Technical report, 1999.

[43] A. Jameson, W. Schmidt, and E. Turkel. Numerical solution of the Euler equations by finite volume methods using Runge Kutta time stepping schemes. In *14th Fluid and Plasma Dynamics Conference*, page 1259, 1981.

[44] A. Aharoni. Demagnetizing factors for rectangular ferromagnetic prisms. *Journal of Applied Physics*, 83(6):3432–3434, 1998.

[45] A. J. Newell, W. Williams, and D. J. Dunlop. A generalization of the demagnetizing tensor for nonuniform magnetization. *Journal of Geophysical Research: Solid Earth*, 98(B6):9551–9555, 1993.

[46] W. Sterk. *Magnetisation characteristics of noncollinear ferromagnetic bilayers*. Bachelor Thesis, Leiden University, 2015.

[47] S. Voltan, C. Cirillo, H. Snijders, K. Lahabi, A. García-Santiago, J. Hernández, C. Attanasio, and J. Aarts. Emergence of the stripe-domain phase in patterned permalloy films. *Physical Review B*, 94(9):094406, 2016.

[48] S. Voltan, A. Singh, and J. Aarts. Triplet generation and upper critical field in superconducting spin valves based on CrO_2. *Physical Review B*, 94(5):054503, 2016.

[49] A. Wachowiak, J. Wiebe, M. Bode, O. Pietzsch, M. Morgenstern, and R. Wiesendanger. Direct observation of internal spin structure of magnetic vortex cores. *Science*, 298(5593):577–580, 2002.

[50] M. Silaev. Possibility of a long-range proximity effect in a ferromagnetic nanoparticle. *Physical Review B*, 79(18):184505, 2009.

[51] A. Singh, C. Jansen, K. Lahabi, and J. Aarts. High-quality CrO_2 nanowires for dissipation-less spintronics. *Physical Review X*, 6(4):041012, 2016.

[52] R. Moriya, L. Thomas, M. Hayashi, Y. B. Bazaliy, C. Rettner, and S. S. Parkin. Probing vortex-core dynamics using current-induced resonant excitation of a trapped domain wall. *Nature Physics*, 4(5):368, 2008.

[53] S. S. Parkin, M. Hayashi, and L. Thomas. Magnetic domain-wall racetrack memory. *Science*, 320(5873):190–194, 2008.

[54] L. Vila, M. Darques, A. Encinas, U. Ebels, J.-M. George, G. Faini, A. Thiaville, and L. Piraux. Magnetic vortices in nanowires with transverse easy axis. *Physical Review B*, 79(17):172410, 2009.

[55] Y. P. Ivanov, A. Chuvilin, L. G. Vivas, J. Kosel, O. Chubykalo-Fesenko, and M. Vázquez. Single crystalline cylindrical nanowires–toward dense 3D arrays of magnetic vortices. *Scientific Reports*, 6:23844, 2016.

[56] M. S. Kalenkov, A. D. Zaikin, and V. T. Petrashov. Triplet superconductivity in a ferromagnetic vortex. *Physical Review Letters*, 107(8):087003, 2011.